PAPER

Check for updates

Carbon/ZrO$_2$ aerogel composite microtube superfoam†

Ding Han, Xiankai Sun, [ID] * Shichao Zhang, Linghao Wu, Bing Ai, Haoran Sun and Yufeng Chen

High-performance thermal insulation materials with broad application prospects have attracted great attention. The introduction of new microstructures into thermal protection materials can significantly improve the thermal insulation performance. The tubular microstructure has obvious advantages such as thermal insulation, lightweight, mechanical, and other properties. Therefore, the microtubular structure has become an important reference microstructure for the development of high-performance thermal insulation materials. In this paper, the carbon/ZrO$_2$ aerogel composite microtube superfoams with excellent thermal protection properties were prepared by a vacuum filtration and high-temperature carbonization method. The ZrO$_2$ aerogel precursor solution can be quickly and uniformly adsorbed on the inner and outer walls of cellulose microtubules. These adsorbed ZrO$_2$ aerogel precursor solution films can be converted into ZrO$_2$ alcohol gel shells under the acceleration and promotion effect of citric acid at 65 °C. The micromorphology of the ZrO$_2$ aerogel shell on the inner and outer walls of the composite microtubes can be efficiently controlled by the concentration of the ZrO$_2$ aerogel precursor solution and the carbonization temperature. The carbon/ZrO$_2$ aerogel composite microtube superfoam exhibits a lower thermal conductivity, lower density, good mechanical properties, and high ablation resistance. The thermal conductivity of the carbon/ZrO$_2$ aerogel composite microtube superfoam is as low as 0.040 ± 0.001 W m^{-1} K^{-1}. The residual rate of the carbon/ZrO$_2$ aerogel composite microtube superfoam is still as high as 84.33% after butane flame ablation for up to 3600 seconds.

1 Introduction

High-performance thermal insulation materials are refractory materials with low thermal conductivity and low heat capacity.[1–3] Due to their significant energy saving and emission reduction effects and excellent thermal insulation performance, the high-performance thermal insulation materials have broad application prospects in construction, transportation, aviation, aerospace, and other fields.[4–6] Therefore, high-performance thermal insulation materials have attracted great attention both from academia and industry.[7,8] Inorganic materials have been widely studied for high-performance thermal insulation materials.[9,10] Carbon materials are a very promising high-temperature insulation material due to their high thermal stability and very low thermal conductivity in high-temperature environments (derived from its high extinction coefficient). However, the fragile and easily oxidized characteristics of carbon materials

limit their wide application in the field of thermal insulation.[11–13] As a kind of inorganic material, Zirconium dioxide (ZrO$_2$) fiber is a widely used high-temperature insulation material due to its the lowest thermal conductivity (among all metal oxides), ultrahigh temperature resistance and long service lifetime.[14,15] However, the thermal insulation properties of zirconia solid fiber have almost no room for further improvement due to their microstructural limitations.[16,17] Therefore, it is necessary to find new microstructures to further improve the thermal insulation properties of ZrO$_2$ materials. Aerogel material is a solid material which is interconnected by nanoparticles to form a nanoscale pore network structure and filled with gas. Aerogel material exhibit many excellent properties including low density, high specific surface area, high porosity, and excellent heat insulation properties.[18–25] The above-mentioned excellent properties of the aerogel material make it an ideal thermal insulation material and has good application prospects in aeronautics, astronautics, and other fields.[26–28] Therefore, introducing an aerogel structure into the new microstructure of ZrO$_2$ materials may further significantly improve the thermal insulation performance of ZrO$_2$ materials.

In nature, the tubular microstructures are widely found in living organisms.[29] This hollow tubular microstructure exhibits

China Building Materials Academy Co., Ltd, No. 1 Guan Zhuang Dong Li, Chaoyang District, Beijing, 100024, P. R. China. E-mail: sunxiankai2008@163.com; tjuhd@163.com; zhangshichao@cbma.com.cn; 16116339@bjtu.edu.cn; aibing2018@163.com; moto398@126.com; chenyunfeng@tom.com; Tel: +86 010-51167551

many excellent properties, such as thermal insulation performance, lightweight performance, impact resistance performance, and mechanical elastic performance.[30,31] These properties of tubular microstructures make microtubular structures is an important reference microstructure for the development of high-performance thermal insulation materials. In fact, the recent research results have shown that ZrO_2 microtubes exhibit more excellent thermal insulation properties because the tubular microstructure restricts the flow of air and induces phonon scattering.[32,33] Therefore, in order to significantly improve the thermal insulation properties of the carbon/ZrO_2 composite thermal insulation materials, we attempted to prepare carbon/ZrO_2 composite thermal insulation materials with a microtube structure. The slender cellulose microtubules are abundant in wood, which can be easily separated from natural wood by using a simple chemical delignification method.[34,35] During the process of removing lignin using chemical methods, a large number of microporous structures are simultaneously introduced into the cellulose microtubules. In addition, there are abundant hydroxyl groups on the inner and outer walls of cellulose microtubules. Therefore, cellulose microtubules exhibit excellent solution adsorption properties. The solution adsorption layers can even form on the inner and outer surfaces of cellulose microtubules. This makes it possible to use the sol–gel method to controllably preparing inorganic aerogel shell materials (such as ZrO_2 aerogel, SiO_2 aerogel and so on) onto the internal and external surfaces of cellulose microtubules. Finally, the composite material, which the cellulose microtubules is controllably coated with the inorganic aerogel material shell, was prepared.

In this study, we are committed to preparing carbon/ZrO_2 aerogel composite microtube superfoam with excellent thermal protection properties. The carbon/ZrO_2 aerogel composite microtube superfoam were prepared by vacuum filtration and high-temperature carbonization method. The micromorphology of the ZrO_2 aerogel shell on the inner and outer walls of the composite microtubes can be efficiently controlled by the concentration of the ZrO_2 aerogel precursor solution and the carbonization temperature. The carbon/ZrO_2 aerogel composite microtube superfoam exhibits a lower thermal conductivity, lower density, good mechanical properties, and high ablation resistance. The thermal conductivity of the carbon/ZrO_2 aerogel composite microtube superfoam is as low as 0.040 ± 0.001 W m^{-1} K^{-1}. The residual rate of the carbon/ZrO_2 aerogel composite microtube superfoam is still as high as 84.33% after butane flame ablation for up to 3600 seconds.

2 Experimental section

2.1 Preparation of the cellulose microtube

About 10 g of poplar sawdust was added to 500 mL of sodium chlorite solution with a mass fraction of 5% at pH 4–5.[36,37] Then the reaction mixture was allowed to stir magnetically at 95 °C for about 12 hours. After the reaction solution was cooled to room temperature and washed several times with deionized water to remove residual chemicals. Finally, the cellulose microtube will be obtained after freeze-drying (Fig. S1†).

2.2 Preparation of the carbon/ZrO_2 aerogel composite microtube superfoam

A certain amount of zirconium oxychloride octahydrate ($ZrOCl_2 \cdot 8H_2O$) and yttrium nitrate hexahydrate ($Y(NO_3)_3 \cdot 6H_2O$) was added to the solution of ethanol (the mass fractions of zirconium oxychloride octahydrate are 2.5%, 5%, 7.5% and 10%, the molar ratios of zirconium to yttrium is 10 : 1). The above mixture was magnetically stirred until a homogeneous transparent liquid was forms (Fig. S2†). A certain amount of citric acid ethanol solution (1 M) was dropped into the above mixed solution and stirred quickly for about 30 seconds to obtain ZrO_2 aerogel precursor solution. 0.5 g of cellulose microtubes were then added to the ZrO_2 aerogel precursor solution and stirred rapidly for 1 min. The cellulose microtubes that evenly adsorbed the ZrO_2 aerogel precursor solution were filtered with Buchner funnel to remove excess ZrO_2 aerogel precursor solution adsorbed by the cellulose microtubes. The obtained cellulose microtubule composite material adsorbed with the ZrO_2 aerogel precursor solution was placed in a closed space at 65 °C for about 6 hours (the ZrO_2 aerogel precursor solution to form a Zr-based alcohol gel shell). The cellulose/Zr-based alcohol gel composite microtubules foam materials were replaced twice with a *n*-hexane solution and dried at 65 °C for 12 hours. Then the cellulose/ZrO_2 aerogel composite microtubules foam materials were obtained after dried at 80 °C for about 6 hours. The dried cellulose/ZrO_2 aerogel composite microtubules foams (Fig. S3†) were carbonized at Y °C for 2 hours in Ar atmosphere (room temperature 400 °C, the heating rate is 1 °C min^{-1}, 400–Y °C, the heating rate is 5 °C min^{-1}, temperature Y is 600, 800, 1000, and 1200 °C). The obtained the carbon/ZrO_2 aerogel composite microtube superfoam was recorded as CZF-X-Y (Y represents the temperature, and X represents the mass fraction of zirconium oxychloride octahydrate). The fabrication process of the CZF-X-Y aerogel composite microtube superfoam material was illustrated in Fig. 1.

2.3 Material characterization

The surface morphologies and the tubular microstructure of the sample were characterized by the field emission scanning electron microscopy (SEM, JSM-6490LV, Japan). The crystal structure of the sample was evaluated using the X-ray diffraction (XRD, D8 ADVANCE, Germany). Raman spectra of the samples were obtained on a HORIBA Scientific LabRAM HR Evolution Raman spectrometer at 532 nm. The surface chemical environment of the sample was studied by X-ray photoelectron spectroscopy (XPS, ESCALAB 250Xi, USA). The mechanical properties of the samples were performed on the electronic universal tensile machine at room temperature (UTM2501, 1000 N load cell, China). Interactions between substances in the sample were characterized using the Fourier transform infrared spectra (FTIR, BRUKER TENSOR 27 FT-IR Spectrometer, Germany). Thermal conductivities of the carbon/ZrO_2 aerogel composite microtube superfoam were evaluated on a DRE-III thermal conductivity meter (Xiangtan Instrument Co., Ltd Xiangtan, China). The adsorption of the zirconium oxychloride octahydrate by the cellulose microtubules was observed using an optical microscope.
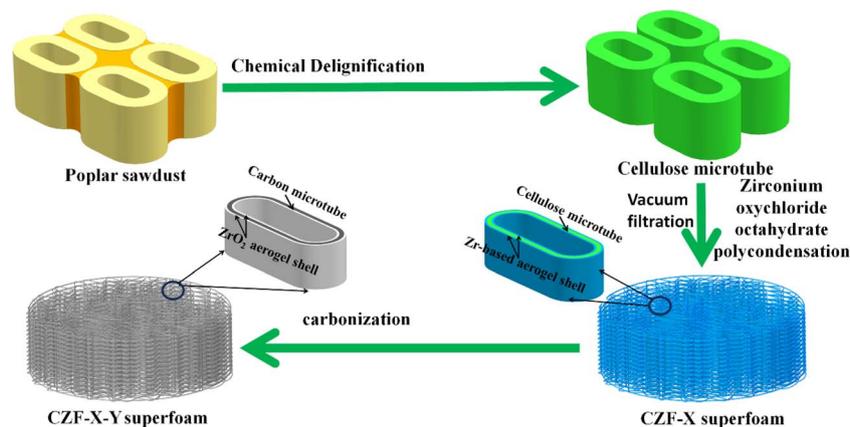
Fig. 1 Illustration of fabrication process for the CZF-*X-Y* aerogel composite microtube superfoam.

3 Results and discussion

The ZrO_2 aerogel precursor solution (mainly containing $[Zr_4(OH)_8 \cdot 16H_2O]^{8+}$, the various complex zirconyl complex species and ethanol) exhibits good wetting properties with cellulose microtubules, which can be quickly adsorbed by cellulose microtubules (Fig. 2a–d). The bubbles trapped in the cellulose microtubules gradually disappeared during the process of adsorbing the ZrO_2 aerogel precursor solution by cellulose microtubules (Fig. S4†). This indicates that ZrO_2 aerogel precursor solution can also be efficiently filled into cellulose microtubules due to the rich pore structure in the wall of the cellulose microtubule and the excellent wettability. Thanks to the pore structure in the wall of the cellulose microtubule, the ZrO_2 aerogel precursor solution filled in the cellulose microtubes will be removed after vacuum filtration using a Buchner funnel. The ZrO_2 aerogel precursor solution was only adsorbed on the wall of cellulose microtubules. The adsorption capacities of the ZrO_2 aerogel precursor solution by the cellulose microtubes filtered through the Buchner funnel were 2.45 ± 0.14 (CZF-2.5), 2.33 ± 0.65(CZF-5.0), 1.76 ± 0.20 (CZF-7.5) and 1.78 ± 0.36 g (CZF-10.0), respectively (Fig. S5†). The ability of cellulose microtubules to adsorb the ZrO_2 aerogel precursor solution gradually decreases as the concentration of the ZrO_2 aerogel precursor solution increases. The amount of citric acid can effectively control the gelation time of the ZrO_2 aerogel precursor solution (1200 to 1 minutes) due to the citric acid altered the gel formation reaction kinetics and promoted the condensation of the zirconyl complex species.[38] Therefore, the amount of citric acid must be precisely controlled to allow the ZrO_2 aerogel precursor solution uniformly adsorbed on the cellulose microtubule wall to form a zirconium-based hydrogel shell before being dried. Fig. 2e–h and S6† shows the SEM images of the CZF-*X* foam. It is obvious that there are no zirconium-based aerogel bulk in the cavities of the cellulose microtubules and the between cellulose microtubules. The tubular microstructure was well preserved. This indicates that the ZrO_2 aerogel precursor solution in the cavity of cellulose microtubules and the between cellulose microtubules can be

effectively removed after vacuum filtration using a Buchner funnel, while only the ZrO_2 aerogel precursor solution film on the cellulose microtubule wall was retained. The zirconium-based aerogel shell uniformly covers the inner and outer walls of cellulose microtubules. The zirconium-based aerogel shell presents a complete monolithic structure. The surface morphology of the zirconium-based aerogel shell did not change significantly with the change of the ZrO_2 aerogel precursor solution. The zirconium-based aerogel shell on the inner and outer surfaces of cellulose microtubules exhibits a relatively dense microtubule morphology (Fig. S7†). Fig. 2i displays the FT-IR spectra of the CZF-*X* foam. The bands at around 671, 558, and 518 cm^{-1} is the Zr–O and Zr–O–Zr stretching vibration peak. The band at about 1061 cm^{-1} in the infrared spectrum of the CZF-*X* foam is the bending vibrations of O–H mixed with Zr–OH bending.[39] The above bands indicate that the polycondensation reaction occurs between the zirconyl complex species in the ZrO_2 aerogel precursor solution film on the cellulose microtubule wall to generate Zr–O–Zr bonds. In addition, it also indicates that the main form of Zr^{4+} ions in ethanol solution is $[Zr_4(OH)_8 \cdot 16H_2O]^{8+}$ complex.[38] The C–O–Zr vibrations band at about 1037 cm^{-1} indicate that there was an interaction between the zirconium-based aerogel and cellulose microtubules. The chemical bonding state of the O and Zr at the zirconium-based complex aerogel shell was further investigated by X-ray photoelectron spectroscopy (Fig. 2j and S8†). The high resolution O 1s spectrum of the CZF-5.0 foam can be fitted into two component peaks.[40] The peak at about 530.5 eV is attributed to lattice oxygen (Zr–O). The peak at about 532.3 eV is attributed to the chemisorbed hydroxyl groups (Zr–OH). The high resolution Zr 3d spectrum of the CZF-5.0 foam shows two peaks at the binding energy of 182.8 and 185.2 eV, which are typical for the Zr^{4+} species in O–Zr–O. The XPS results further prove that the polycondensation reaction occurs between the zirconyl complex species in the ZrO_2 aerogel precursor solution film on the cellulose microtubule wall to generate the zirconium-based aerogel shell. The compressive stress–strain curves of the CZF-*X* foams are shown in Fig. 2k. It is obvious that the mechanical strength of the CZF-*X* foams gradually increases as the concentration of the ZrO_2 aerogel precursor solution increases.

In the low strain range, the stress–strain behaviour of the CZF-X foams was linear elasticity originating from the elastic bending of the composite microtubules. After the yield stress, the stress–strain curves entered a plateau region with a slowly increasing stress, which was caused by the plastic yielding of the composite microtubules. At 60% strain, the stress value of the CZF-X foams was increased from 32.8 kPa for the CZF-2.5 foam to 148.6 kPa for the CZF-10 foam. Subsequently, the stress of the CZF-X foams rises sharply with strain duo to the densification of the CZF-X foams at higher strain. The CZF-X foams have a smaller density due to the hollow microtube structure (Fig. 2l). The density of the CZF-2.5 foam is only 42.8 ± 14.7 kg m^{-3}.

The carbon/ZrO$_2$ aerogel composite microtube superfoams were prepared by carbonizing CZF-X foams at different temperatures in an argon atmosphere (Fig. S9 and S10†). Fig. 3a–h and S11† are the SEM images of the CZF-5.0-Y aerogel composite microtube superfoams. The tubular microstructure of cellulose microtubules is preserved in the CZF-5.0-Y aerogel composite microtube superfoams. The ZrO$_2$ aerogel shells on the inner and outer walls of the carbon/ZrO$_2$ composite microtube exhibit a uniform and complete monolithic structure. The obviously wrinkled morphology does not appear in the ZrO$_2$ aerogel shell of the carbon/ZrO$_2$ composite microtube. In addition, there is no obvious separation between the carbon shell and the ZrO$_2$ aerogel shell in the carbon/ZrO$_2$ composite microtubules. At carbonization temperatures of 600, 800, and 1000 °C. The ZrO$_2$ aerogel shell is assembled from ZrO$_2$ nanoparticles. However, the nanoparticle microstructure of ZrO$_2$ on the ZrO$_2$ aerogel shell was not obvious at the carbonization temperature of 1200 °C. The crystal structure and phase of the CZF-5.0-Y aerogel composite microtube superfoams at different carbonization temperatures were characterized by X-ray diffraction (XRD). The XRD patterns of the CZF-5.0-Y aerogel composite microtube superfoams were shown in Fig. 3i. The characteristic peaks at around 29.8°, 34.5°, 34.9°, 49.9°, 59.2°, 59.8°, 62.4°, 73.1° and 74.1° can be assigned to the (011), (002), (110), (112), (013), (121), (202), (004) and (220) crystal planes of the tetragonal ZrO$_2$ (t-ZrO$_2$, JCPDS card no. 50-1089). The tetragonal crystal phase of ZrO$_2$ can be stable at room temperature duo to the addition of Y^{3+} ions. The addition of larger Y^{3+} ions increase the r$^+$/r$^-$ ratio, thereby making the tetragonal ZrO$_2$ phase more stable at room temperature. When Y^{3+} ions are introduced into the ZrO$_2$ lattice, the oxygen vacancies are also introduced into the ZrO$_2$ lattice to ensure electrical neutrality, which can reduce the electrostatic repulsion between the adjacent O^{2-} ions, cause greater lattice distortion and releases some of the interlaminar stress, thus making the tetragonal ZrO$_2$ phase more stable at room temperature.[41] It can be observed that the crystal structure of the ZrO$_2$ in the CZF-5.0-Y aerogel composite microtube superfoams materials at different carbonization temperatures is t-ZrO$_2$, meaning that the carbonization temperature did not affect phase composition of
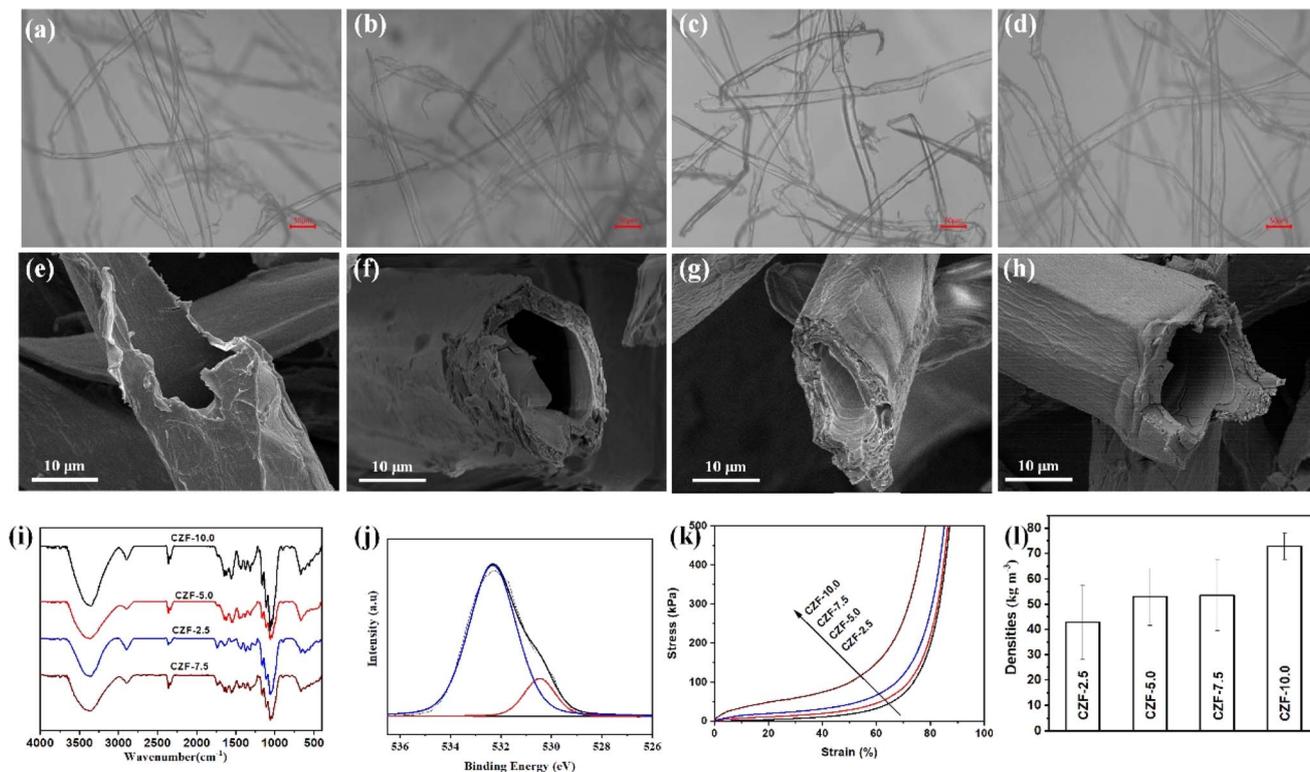

Fig. 2 Optical images of the cellulose microtubes after saturated adsorption of the ZrO$_2$ aerogel precursor solution with different concentrations (a) CZF-2.5 foam, (b) CZF-5.0 foam, (c) CZF-7.5 foam, and (d) CZF-10.0 foam, SEM images of the (e) CZF-2.5 foam, (f) CZF-5.0 foam, (g) CZF-7.5 foam, and (h) CZF-10.0 foam, the FT–IR spectra of the CZF-X foam (i), the high resolution O 1s spectrum of the CZF-5.0 foam (j), the mechanical strength of the CZF-X foam (k), the density of the CZF-X foam (l).

the CZF-5.0-Y aerogel composite microtube superfoams. The X-ray photoelectron spectroscopy (XPS) was applied to further get surface information of the CZF-5.0-1000 aerogel composite microtube superfoams. The high-resolution O 1s, Zr 3d and C 1s peaks are shown in Fig. 3j and S12,† respectively. The deconvoluted O 1s spectrum shows the presence of three different oxygen groups: the lattice oxygen under completely oxidized stoichiometric conditions (O–Zr–O) at 530.4 eV, the adsorbed oxygen species in the oxygen deficient regions (V_O) at 531.0 eV, and the chemisorbed hydroxyl groups (Zr–OH) at 532.7 eV. The oxygen vacancies in the the carbon/ZrO_2 composite microtubules originate from the introduction of the Y^{3+} ions and the inert carbonization atmosphere. The high resolution Zr 3d spectrum of the CZF-5.0-1000 aerogel composite microtube superfoams can be deconvoluted into two peaks centered at 182.7 and 185.1 eV, which are typical for the Zr^{4+} species in O–Zr–O. The high-resolution C 1s spectrum of the CZF-5.0-1000 aerogel composite microtube superfoams shows four peaks: C–C/C=C (centered at 284.8 eV), C–O (centered at 285.7 eV), C=O (centered at 286.7 eV), and O–C=O (centered at 289.2 eV). The Raman spectra of the CZF-5.0-Y aerogel composite microtube superfoams show two peaks around at 1349 and 1615 cm^{-1} (Fig. S13†), which are related to D-band (disordered carbon) and G-band (graphitized carbon), respectively.[42] The I_D/I_G ratio of the CZF-5.0-X aerogel composite microtube superfoams is 0.798 (CZF-5.0-600), 0.995 (CZF-5.0-800), 1.002 (CZF-5.0-1000), and 1.008 (CZF-5.0-1200), respectively. The I_D/I_G ratio gradually increases with increasing temperature. It shows that the degree of disorder in the CZF-5.0-Y aerogel composite microtube superfoams becomes larger with the carbonization temperature increases within the carbonization temperature studied. Fig. S14† show the nitrogen adsorption/desorption isotherm and pore size distribution curve of CZF-5.0-Y superfoam and the relevant pore structure parameters of CZF-5.0-Y superfoam are summarized in Table S1.† According to the IUPAC classification, the nitrogen adsorption/desorption isotherm of CZF-5.0-Y superfoam belongs to the type I nitrogen adsorption/desorption isotherm with H4 type hysteresis loop. This shows that there are many micropores in CZF-5.0-Y superfoam, and the pore diameter is mainly distributed around 3.5 nm. When the carbonization temperature gradually increases from 600 °C to 1000 °C, the specific surface area rapidly increases from 20 m^2 g^{-1} of CZF-5.0-600 superfoam to 494 m^2 g^{-1} of CZF-5.0-1000 superfoam. When the carbonization temperature further increased to 1200 °C, the specific surface area of CZF-5.0-1200 superfoam decreased to 353 m^2 g^{-1}. CZF-5.0-600 superfoam has the smallest total pore volume (only 0.0234 cm^3 g^{-1}) and the largest average pore diameter (about 4.5 nm). However, CZF-5.0-1000 superfoam has a total pore volume as high as 0.2717 cm^3 g^{-1}. The average pore diameter of the CZF-5.0-1000 superfoam is approximately 2.2 nm. The compressive stress–strain curves of the CZF-5.0-Y aerogel composite microtube superfoams are shown in Fig. 3k. Obviously, the CZF-5.0-600 aerogel composite microtube superfoams exhibit better mechanical properties among the CZF-5.0-Y aerogel composite microtube superfoams. The possible reason is that the CZF-based aerogel composite microtube superfoams cannot be completely carbonized at 600 °C. In the temperature range of 800–1200 °C, the mechanical properties of the CZF-based aerogel composite microtube superfoams gradually increase with the carbonization temperature increases. The density of the CZF-5.0-Y aerogel composite microtube superfoams increases slightly with the temperature decreases from 1200 to 800 °C (Fig. S15†). The density of the CZF-based aerogel composite microtube superfoams is as low as 28.4 ± 1.7 kg m^{-3} (CZF-5.0-1200), which is even an order of magnitude lower than the reported density of foam materials.[43,44] When the carbonization temperature is 600 °C, the density of the CZF-5.0-600 aerogel composite microtube superfoams increases significantly to 52.4 ± 6.9 kg m^{-3}. This further indicates that the CZF-Y foam cannot be completely carbonized at 600 °C. The thermal conductivity of the CZF-5.0-Y aerogel composite microtube superfoams is 0.038 ± 0.002, 0.040 ± 0.001, 0.039 ± 0.002, and 0.044 ± 0.002 W m^{-1} K^{-1}, which is superior to the reported thermal conductivity of the ZrO_2/carbon composites.[45,46] The slightly difference in thermal conductivity of the CZF-5.0-Y aerogel composite microtube superfoams indicates that the carbonization temperature has little effect on the thermal insulation performance of the CZF-5.0-Y aerogel composite microtube superfoams.

The morphology and microstructure of the CZF-X-1000 aerogel composite microtube superfoams were shown in Fig. 4a–d and S16.† It is obvious that the micromorphology of the ZrO_2 aerogel shell on the inner and outer walls of the carbon/ZrO_2 composite microtube changes significantly with the concentration of the ZrO_2 aerogel precursor solution increases. When the concentration of the ZrO_2 aerogel precursor is about 2.5%, the ZrO_2 aerogel shell is composed of randomly stacked smaller ZrO_2 nanoparticles. In addition, there are a large number of nanopore structures in the ZrO_2 aerogel shell. When the concentration of the ZrO_2 aerogel precursor increases to 5.0%, the size of the ZrO_2 nanoparticles used to construct the ZrO_2 aerogel shell has become larger. At the same time, the pore structure in the ZrO_2 aerogel shell has become smaller. When the concentration of the ZrO_2 aerogel precursor is further increased to 7.5%, the size of ZrO_2 nanoparticles becomes significantly larger. These large-sized ZrO_2 nanoparticles are closely packed together to form a ZrO_2 aerogel shell. When the concentration of the ZrO_2 aerogel precursor is about 10.0%, the size of ZrO_2 nanoparticles becomes small instead. These small-sized ZrO_2 nanoparticles accumulate into a denser ZrO_2 aerogel shell. The tubular microstructure of cellulose microtubules in the CZF-X-1000 aerogel composite microtube superfoams can be effectively retained when the concentration of the ZrO_2 aerogel precursor increases from 2.5% to 10.0%. The ZrO_2 aerogel within or between microtubules of the CZF-X-1000 aerogel composite microtube superfoams was not found. The ZrO_2 aerogel shell and carbon microtubules interact closely with each other without obvious separation. The ZrO_2 aerogel shell presents a uniform and complete structure on the inner and outer walls of the carbon/ZrO_2 composite microtube. The concentration of the ZrO_2 aerogel precursor has a significant impact on the mechanical properties of the CZF-X-1000 aerogel composite microtube superfoams. Fig. S17† show the nitrogen adsorption/desorption isotherm and pore size distribution curve of CZF-X-
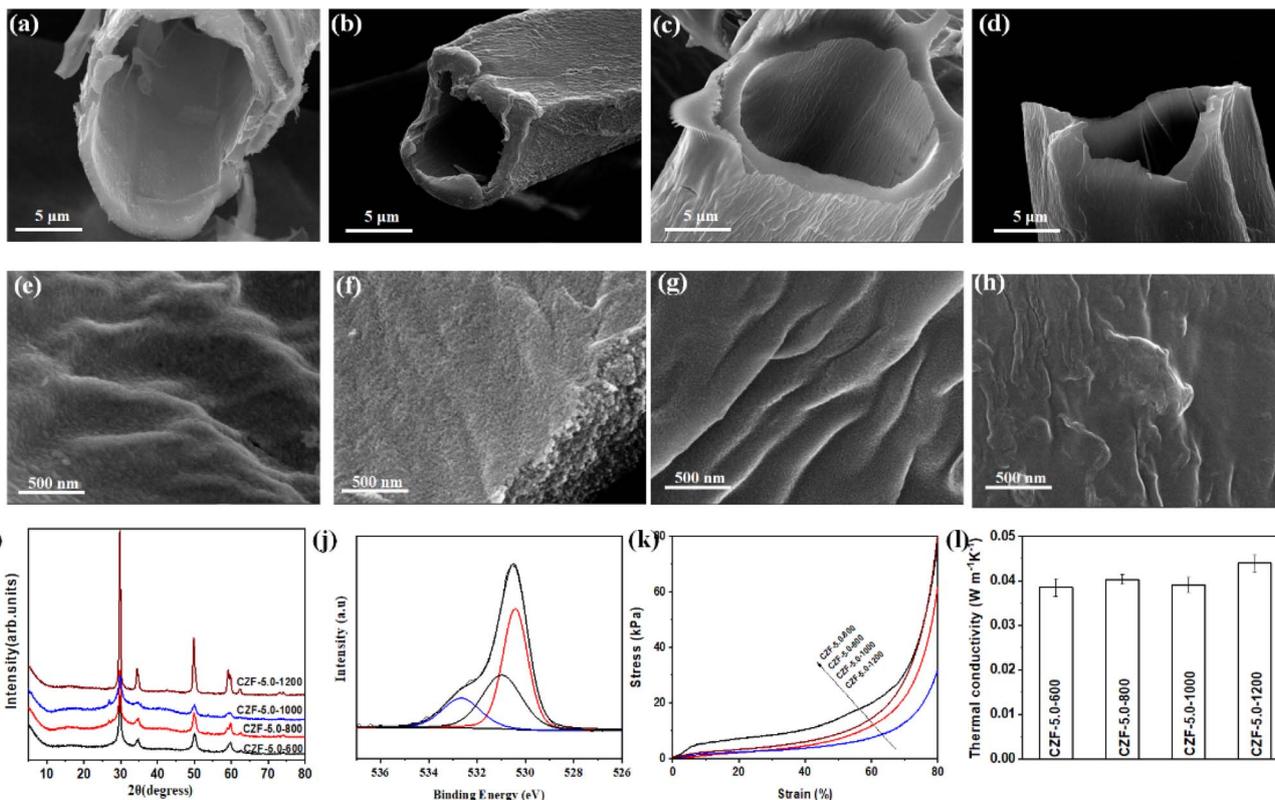
Fig. 3 SEM image of the CZF–5.0–Y superfoam (a) and (e) CZF–5.0–600, (b) and (f) CZF–5.0–800, (c) and (g) CZF–5.0–1000, (d) and (h) CZF–5.0–1200; XRD pattern (i) of the CZF–5.0–Y superfoam, the high-resolution O 1s spectrum of the CZF–5.0–1000 superfoam (j), the mechanical strength (k) and the thermal conductivity (l) of the CZF–5.0–Y superfoam.

1000 superfoam and the relevant pore structure parameters of CZF-X-1000 superfoam are summarized in Table S2.† The nitrogen adsorption/desorption isotherm of CZF-X-1000 superfoam belongs to the type I nitrogen adsorption/desorption isotherm with H4 type hysteresis loop (according to IUPAC classification). The pore structure of CZF-X-1000 superfoam is mainly composed of micropores, and its pore diameter is mainly distributed around 3.7 nm. The specific surface area of CZF-2.5-1000 superfoam is as high as 796 m^2 g^{-1}. When the concentration of ZrO$_2$ aerogel precursor solution gradually increased to 7.5%, the specific surface area of CZF-7.5-1000 superfoam decreased to 188 m^2 g^{-1}. However, when the concentration of the ZrO$_2$ aerogel precursor solution further increased to 10.0%, the specific surface area of CZF-10.0-1000 superfoam increased slightly to 198 m^2 g^{-1}. The total pore volume of CZF-X-1000 superfoam gradually decreases as the ZrO$_2$ aerogel precursor solution concentration increases. The total pore volume of CZF-2.5-1000 superfoam is as high as 0.4541 cm^3 g^{-1}, while the total pore volume of CZF-10.0-1000 superfoam is only 0.1412 cm^3 g^{-1}. The average pore diameters of CZF-2.5-1000, CZF-5.0-1000, CZF-7.5-1000 and CZF-10.0-1000 superfoams are 2.3, 2.2, 3.1 and 2.8 nm respectively. Fig. 4e shows the compressive stress–strain curves of the CZF-X-1000 aerogel composite microtube superfoams. The compressive strength of the CZF-X-1000 aerogel composite microtube superfoams gradually increases with the increase of the

concentration of the ZrO$_2$ aerogel precursor. The compressive strength increased from 6.48 kPa for the CZF-2.5-1000 aerogel composite microtube superfoams to 23.36 kPa for the CZF-10.0-1000 aerogel composite microtube superfoams under the strain of 60%. The mechanical properties of the CZF-Y-1000 aerogel composite microtube superfoams indicate that ZrO$_2$ aerogel shell can effectively improve the mechanical properties of the CZF-X-1000 aerogel composite microtube superfoams, and the microstructure of ZrO$_2$ aerogel shell significantly affects the mechanical properties of foam materials. The CZF-X-1000 aerogel composite microtube superfoams exhibit good thermal insulation properties (Fig. 4f). The thermal conductivity of the CZF-X-1000 aerogel composite microtube superfoams is 0.042 ± 0.001 (CZF-2.5-1000), 0.040 ± 0.003 (CZF-5.0-1000), 0.040 ± 0.001 (CZF-7.5-1000), and 0.046 ± 0.003 W m^{-1} K^{-1} (CZF-10.0-1000), respectively.

The color of the ablated surface changed from black to white after the CZF-X-Y aerogel composite microtube superfoams was ablated by butane flame for 3600 s (Fig. 5). This indicates that the structural unit of the CZF-X-Y aerogel composite microtube superfoams is transformed from carbon/ZrO$_2$ composite microtubules into ZrO$_2$ microtubules along with the ablation process (Fig. S18†). Although the structural units of the CZF-X-Y aerogel composite microtube superfoams change during the butane flame ablation process, the butane flame gas flow cannot cause materials (such as ZrO$_2$ microtubes or carbon/
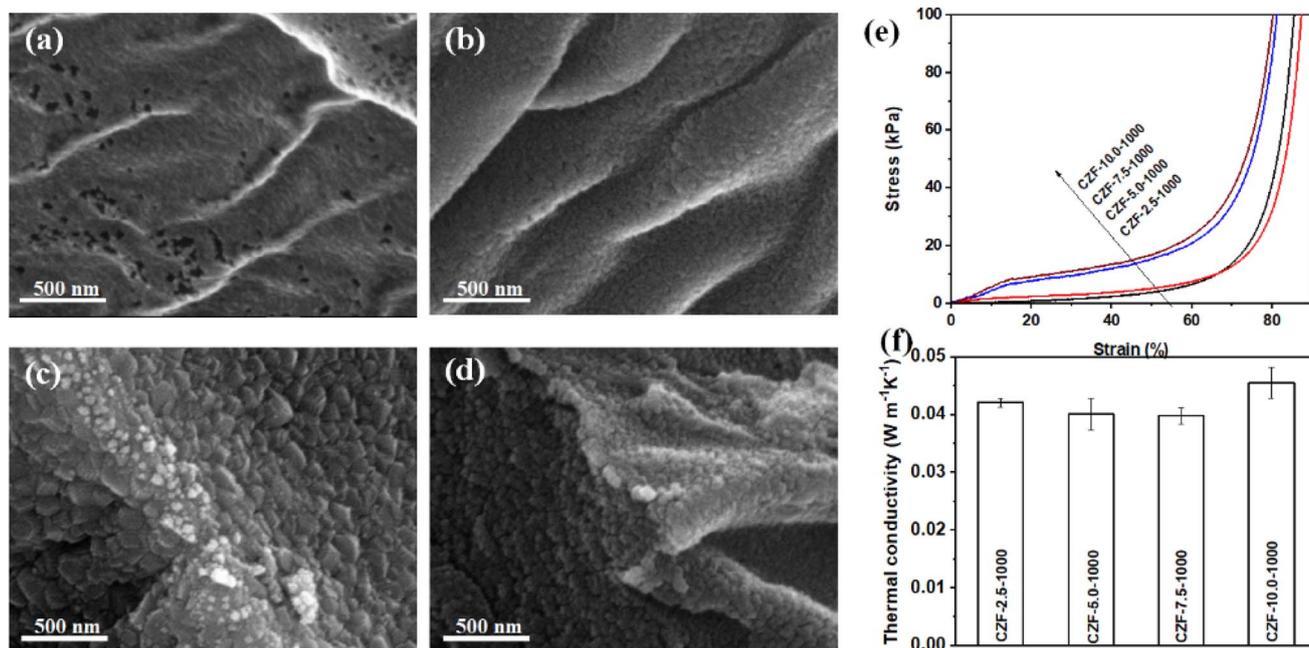
Fig. 4   SEM image of the CZF-*X*-1000 aerogel composite microtube superfoams (a) CZF-2.5-1000, (b) CZF-5.0-1000, (c) CZF-7.5-1000, (d) CZF-10.0-1000; the mechanical strength (e) and the thermal conductivity (f) of the CZF-*Y*-1000 aerogel composite microtube superfoams.

ZrO$_2$ composite microtubules) to fall off from the ablated surface of the CZF-*X-Y* aerogel composite microtube superfoams. This indicates that the three-dimensional microtubule structure of the CZF-*X-Y* superfoam with good mechanical strength can be completely maintained during and after the conversion process of the CZF-*X-Y* aerogel composite microtube superfoams structural units. In addition, another reason is that the ZrO$_2$ aerogel shell of the carbon/ZrO$_2$ composite microtubules in the tetragonal crystal phase at room temperature. Obviously, although the ablated surface of the CZF-*X-Y* superfoam was ablated by the butane flame for up to 3600 s, the white only appeared near the ablated surface. The possible reason is that the low thermal conductivity of the CZF-*X-Y* aerogel composite microtube superfoams provides excellent thermal insulation properties, and the composite tubular microstructure can significantly improve the stability of the middle carbon layer in an aerobic high-temperature environment. When the carbonization temperature is 1200 °C or the concentration of the ZrO$_2$ aerogel precursor is 10%, the ablated surface (the CZF-5.0-1200 and CZF-10.0-1000 aerogel composite microtube superfoam) that has been ablated by butane flame for 3600 seconds still has a certain black. This indicates that the carbon materials are tightly wrapped in the microtube structural units of the CZF-5.0-1200 and CZF-10.0-1000 aerogel composite microtube superfoam has excellent stability in high-temperature aerobic environments. The possible reason is that increasing the carbonization temperature or increasing the concentration of the ZrO$_2$ aerogel precursor can lead to denser
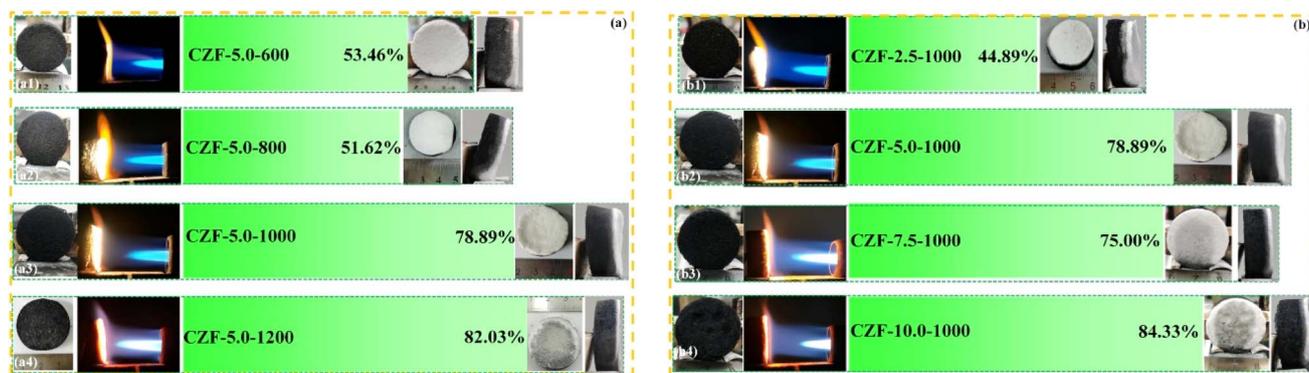

Fig. 5   The ablation resistance of the CZF-5.0-*Y* (a) and the CZF-*X*-1000 aerogel composite microtube superfoams (b) under the flame of butane blowtorch (photos of the ablated surface of the superfoam before being ablated by butane flame, photos of the ablated surface and side of the superfoam after being ablated by butane flame for 3600 s, and the residual rate of the foam after being ablated by butane flame for 3600 s).

ZrO$_2$ aerogel shell, and enhance the barrier to oxygen penetration. Therefore, the stability of the carbon material wrapped in the microtube structural units of the CZF-X-Y aerogel composite microtube superfoam becomes better in a high-temperature aerobic environment. When the concentration of the ZrO$_2$ aerogel precursor solution is 5.0%, the residual rate of the CZF-X-Y aerogel composite microtube superfoam after ablation increases from 53.46% (the CZF-5.0-600 aerogel composite microtube superfoam) to 82.03% (the CZF-5.0-1200 aerogel composite microtube superfoam) with the carbonization temperature increases from 600 to 1200 °C. In addition, the residual rate of the CZF-X-Y aerogel composite microtube superfoam after ablation increases from 44.89% (the CZF-2.5-1000) to 84.33% (the CZF-10.0-1000) with the concentration of the ZrO$_2$ aerogel precursor solution increases from 2.5% to 10.0% when the carbonization temperature is 1000 °C.

4 Conclusions

In conclusion, the carbon/ZrO$_2$ aerogel composite microtube superfoams with excellent thermal protection properties were prepared by vacuum filtration and high-temperature carbonization method. The ZrO$_2$ aerogel precursor solution can be quickly and uniformly adsorbed on the inner and outer walls of cellulose microtubules. These adsorbed ZrO$_2$ aerogel precursor solution film can be converted into ZrO$_2$ alcohol gel shells under the acceleration and promotion effect of citric acid at 65 °C. The micromorphology of the ZrO$_2$ aerogel shell on the inner and outer walls of the composite microtubes can be efficiently controlled by the concentration of the ZrO$_2$ aerogel precursor solution and the carbonization temperature. The carbon/ZrO$_2$ aerogel composite microtube superfoam exhibits a lower thermal conductivity, lower density, good mechanical properties, and high ablation resistance. The thermal conductivity of the carbon/ZrO$_2$ aerogel composite microtube superfoam is as low as 0.040 ± 0.001 W m^{-1} K^{-1}. The residual rate of the carbon/ZrO$_2$ aerogel composite microtube superfoam is still as high as 84.33% after butane flame ablation for up to 3600 seconds.

Data availability

The authors declare that the data and materials were available.

Author contributions

DH and XS: idea for the article, literature search and analysis, experiment, writing and revision of the manuscript. SZ: literature search and experiment. LW: idea for the article, analysis, revision of the manuscript. BA: analysis, revision of the manuscript. HS: experimental protocol design. YC: revision of the manuscript.

Conflicts of interest

The authors declare no competing interests.

References

1 T. Nakaya, M. Yamasaki, S. Fukuta and Y. Sasaki, *For. Prod. J.*, 2016, **66**, 300–307.

2 L. Cosentino, J. Fernandes and R. Mateus, *Energies*, 2023, **16**, 4676.

3 K. H. Lee, Z. Arshad, A. Dahshan, M. Alshareef, Q. A. Alsulami, A. Bibi, E.-J. Lee, M. Nawaz, U. Zubair and A. Javid, *Catalysts*, 2023, **13**, 1286.

4 I. Cetiner and A. D. Shea, *Energy Build.*, 2018, **168**, 374–384.

5 D. Kang, S. Yun and B.-k. Kim, *Energies*, 2022, **15**, 4357.

6 R. Jin, Z. Zhou, J. Liu, B. Shi, N. Zhou, X. Wang, X. Jia, D. Guo and B. Xu, *Gels*, 2023, **9**, 606.

7 J. Lyu, Z. Liu, X. Wu, G. Li, D. Fang and X. Zhang, *ACS Nano*, 2019, **13**, 2236–2245.

8 L. Aditya, T. M. I. Mahlia, B. Rismanchi, H. M. Ng, M. H. Hasan, H. S. C. Metselaar, O. Muraza and H. B. Aditiya, *Renewable Sustainable Energy Rev.*, 2017, **73**, 1352–1365.

9 Y. O. Perminov, A. A. Lysenko, E. S. Sveshnikova and O. V. Astashkina, *Fibre Chem.*, 2016, **48**, 235–238.

10 T. Zhou, Y. Xu, Y. Zhen, K. Wu, H. Ding, L. Wang, X. Tai, X. Cai, X. Zhang, T. Xia, J. Zhu, W. Chu, Y. Ni, Y. Xie and C. Wu, *Adv. Mater.*, 2023, 2306135, DOI: **10.1002/adma.202306135**.

11 M. Guo, J. Li, K. Xi, Y. Liu and J. Ji, *Acta Astronaut.*, 2019, **159**, 508–516.

12 L. Hu, R. He, H. Lei and D. Fang, *Int. J. Thermophys.*, 2019, **40**, 1–25.

13 J.-H. Lee and S.-J. Park, *Carbon*, 2020, **163**, 1–18.

14 Z. Xu, F. Wang, X. Yin, L. Cheng, J. Yu, Y. Liu and B. Ding, *Sci. China Mater.*, 2023, **66**, 421–440.

15 Y. A. Balinova, N. M. Varrik, A. V. Istomin and G. Y. Lyulyukina, *Fibre Chem.*, 2018, **50**, 10–18.

16 T. Wang, Q. Yu, J. Kong and C. Wong, *Ceram. Int.*, 2017, **43**, 9296–9302.

17 X. Pang, T. Wang and J. Kong, *Ceram. Int.*, 2020, **46**, 9103–9108.

18 Z. Di, S. Ma, H. Wang, Z. Guan, B. Lian, Y. Qiu and Y. Jiang, *Coatings*, 2022, **12**, 1421.

19 M. Wang, J. Feng, Y. Jiang, Z. Zhang and J. Feng, *Heat Mass Transfer*, 2018, **54**, 2793–2798.

20 M. Li, X. Chen, X. Li, J. Dong, C. Teng, X. Zhao and Q. Zhang, *Compos. Commun.*, 2022, **35**, 101346.

21 G. Tao, J. Wu and M. Zhu, *Adv. Fiber Mater.*, 2024, 1–3, DOI: **10.1007/s42765-024-00376-x**.

22 Y. X. Chen and Q. Yu, *Constr. Build. Mater.*, 2024, **411**, 134478.

23 W. Nasri, R. Djebali, A. J. Chamkha, A. Bezazi, F. Mechighel, P. Reis and Z. Driss, *J. Appl. Comput. Mech.*, 2024, **10**, 140–151.

24 M. Lin, H. Sun, Y. Chen and J. Chen, *Packag. Technol. Sci.*, 2024, **37**, 85–95.

25 F. Lou, S. Dong, K. Zhu, X. Chen and Y. Ma, *Gels*, 2023, **9**, 220.

26 N. Bheekhun, A. R. Abu Talib and M. R. Hassan, *Adv. Mater. Sci. Eng.*, 2013, **2013**, 406065.

27 A. V. Rao, *J. Sol–Gel Sci. Technol.*, 2019, **90**, 28–54.

28 R. C. Walker, A. E. Potochniak, A. P. Hyer and J. K. Ferri, *Adv. Colloid Interface Sci.*, 2021, **295**, 102464.

29 A. S. Wu, J. E. Oldfield and J. Adair, *J. Anim. Sci.*, 1977, **44**, 462–466.

30 J. Sun, Z. Wu, C. Ma, M. Xu, S. Luo, W. Li and S. Liu, *J. Mater. Chem. A*, 2021, **9**, 13822–13850.

31 J. Sun, Z. Wu, B. An, C. Ma, L. Xu, Z. Zhang, S. Luo, W. Li and S. Liu, *Composites, Part B*, 2021, **220**, 108997.

32 S. Zhen, W. Sun, G. Tang, D. Rooney, K. Sun and X. Ma, *Ceram. Int.*, 2016, **42**, 8559–8564.

33 X. Liu, T. Wang, J. Kong and C. Wong, *Ceram. Int.*, 2021, **47**, 8685–8691.

34 Q. Tang, L. Fang, Y. Wang, M. Zou and W. Guo, *Nanoscale*, 2018, **10**, 4344–4353.

35 K. Gao, J. Song, Q. Niu, Q. Tang, X. Sun and L. Wang, *J. Mater. Sci.*, 2023, 13009–13018, DOI: **10.1007/s10853-023-08837-1**.

36 Q. Niu, Q. Tang, X. Sun, L. Wang and K. Gao, *J. Mater. Sci.*, 2022, **57**, 5154–5166.

37 Q. Niu, H. Zhang, K. Gao, Q. Tang, X. Sun, S. Zhao and L. Wang, *Chemnanomat*, 2022, **8**, e202200001.

38 Z. Zhang, Q. Gao, Y. Liu, C. Zhou, M. Zhi, Z. Hong, F. Zhang and B. Liu, *RSC Adv.*, 2015, **5**, 84280–84283.

39 C. Liu, K. Li, H. Li, S. Zhang, Y. Zhang and X. Hou, *J. Mater. Sci.*, 2015, **50**, 2824–2831.

40 Q. Chen, W. Yang, J. Zhu, L. Fu, D. Li and L. Zhou, *J. Mater. Sci.: Mater. Electron.*, 2019, **30**, 701–710.

41 N. Gupta, P. Mallik, M. H. Lewis and B. Basu, in *Euro Ceramics VIII, Pts 1–3*, ed. H. Mandal and L. Ovecoglu, 2004, vol. 264–268, p. 817.

42 L. Hu, J. Hou, Y. Ma, H. Li and T. Zhai, *J. Mater. Chem. A*, 2016, **4**, 15006–15014.

43 A. Jung, G. Falk, D. Petri and S. Diebels, *Mech. Mater.*, 2015, **82**, 13–27.

44 H. Mohseni and T. W. Scharf, *J. Vac. Sci. Technol., A*, 2012, **30**, 01A149.

45 M. Wisniewska, A. M. Laptev, M. Marczewski, V. Leshchynsky, G. Lota, I. Acznik, L. Celotti, A. Sullivan, M. Szybowicz and D. Garbiec, *Ceram. Int.*, 2023, **49**, 15442–15450.

46 Z. Niu, B. Chen, S. Shen, H. Zhang, X. Ma, F. Chen, L. Li, Y. Xin, C. Zhang and X. Hou, *Compos. Commun.*, 2022, **35**, 101284.